Angewandte Communications

DOI: 10.1002/anie.201208993

Electrochemistry

Enhanced Supercapacitor Performance of MnO_2 by Atomic Doping**

*Jianli Kang, Akihiko Hirata, Lijing Kang, Xianmin Zhang, Ying Hou, Luyang Chen, Cheng Li, Takeshi Fujita, Kazuto Akagi, and Mingwei Chen**

Since the first report on the supercapacitor behavior of manganese dioxide (MnO_2) in 1999,[1] MnO_2 has been one of the most promising active materials for electrochemical capacitors because of its high theoretical capacitance ($1370\,F\,g^{-1}$), low costs, environmental friendliness, and natural abundance. Nevertheless, the high specific capacitance of MnO_2 can only be realized in the form of low-dimensional thin films (tens of nanometers) and small nanoparticles with a low loading amount ($< 10\,\mu g\,cm^{-2}$).[2] Increasing the loading amount to a critical value of about $10\,\mu g\,cm^{-2}$ leads to dramatic loss of specific capacitance and only less than 30 % of the theoretical value (about 100–300 $F\,g^{-1}$) can be retained because of the intrinsically low conductivity (10^{-5}–$10^{-6}\,S\,cm^{-1}$) of MnO_2.[3] Apparently, the low capacity from thin or thick films with low specific capacitance is one of the key factors that limit practical applications of MnO_2 as a high-performance pseudo-capacitive material. To address this problem, MnO_2-based composites with conductive materials, such as carbon, conducting polymers,[4] nanoporous metals,[5] and conductive metal oxides,[6] have been intensely studied recently. However, the enhancement of MnO_2 conductivity by the external conductive reinforcements is very limited because of the restriction of the MnO_2/conductor interfaces. Doping can improve the performance of oxides.[7] However, previous works are mainly focused on metal cations/MnO_2 systems and the resultant improvement in electronic conductivity and capacitance is obscure.

Herein, we propose a novel approach to improving the capacitive performance of thick MnO_2 films by enhancing the intrinsic conductivity of MnO_2 using non-equilibrium doping of free electron metal atoms (such as Au, Ag, Cu, and so on). The free electron metal atoms as electron donors are expected to change the electronic structure of MnO_2 for a better conductivity and high capacitive performance. To verify this idea, in this study we take the Au-doped porous MnO_2 as an example. The fabrication process is described in Figure 1 a. A 350 nm thick porous MnO_2 layer was first electrochemically deposited on a 100 nm thick nanoporous gold (NPG) material which has been shown to be an excellent current collector.[5a] Au atoms were then doped in MnO_2 by physical vapor deposition (PVD) using a sputtering coater. By repeating the two steps, a thick Au-doped MnO_2 film was obtained.

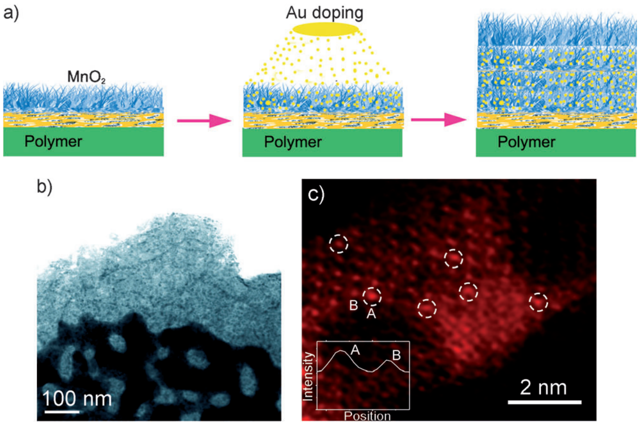

Figure 1. a) Fabrication process of the Au-doped MnO_2 electrodes. b,c) STEM images of the Au-doped MnO_2. The inset of (c) indicates the intensity difference between Au-occupied columns and undoped Mn–O atomic columns.

Figure 1 b shows the scanning transmission electron microscopy (STEM) image of the Au-doped MnO_2 film with a thickness of about 1.35 μm. The Au concentration in the sample is about 9.9 at. %, approximately determined by energy dispersive X-ray spectroscopy (EDS). The high-angle annular dark-field (HAADF) STEM image indicates that most of the doped Au atoms are homogeneously distributed in the MnO_2 lattice in the form of individual atoms except for a small number of gold nanoparticles (Figure 1 c). The atomic doping is also confirmed by X-ray diffraction experiments as shown in Figure S2 in the Supporting Information. The detectable diffraction peak shift, corresponding to an increased lattice constant by Au doping, provides the solid evidence that the doped Au atoms indeed get into the MnO_2 lattice, rather than on the sample surface.

The electronic structure of Au-doped and undoped MnO_2 was investigated by X-ray photoelectron spectroscopy (XPS). Figure S3 shows that the Mn 2p peaks become much broader and a peak splitting is detectable after Au doping. The peak splitting is probably associated with the emergence of the doped Au 4p peak. Meanwhile, the mean valence of Mn, calculated from the areas under each deconvoluted peak, changes from 3.3 to 2.8 after Au doping. Figure S3 b shows O 1s spectra taken from pure and Au-doped MnO_2. The O 1s

---

[*] Dr. J. L. Kang, Dr. A. Hirata, L. J. Kang, Dr. X. Zhang, Y. Hou, Dr. L. Y. Chen, C. Li, Dr. T. Fujita, Dr. K. Akagi, Prof. M. W. Chen
WPI Advanced Institute for Materials Research, Tohoku University
Sendai, 980-8577 (Japan)
E-mail: mwchen@wpi-aimr.tohoku.ac.jp
Prof. M. W. Chen
CREST (Japan) Science and Technology Agency (JST)
Saitama, 332-0012 (Japan)

[**] This work is sponsored by JST-CREST "Phase Interface Science for Highly Efficient Energy Utilization", JST (Japan).

Supporting information for this article is available on the WWW under http://dx.doi.org/10.1002/anie.201208993.

spectra can be deconvoluted into three components corresponding to Mn−O−Mn, Mn−O−H, and H−O−H bonds. The relative fraction of each O bonding state is given in Table S1. Au doping induces a higher hydration of manganese oxide. Additionally, two Au 4f bonding-energy peaks at 84.49 and 88.16 eV also shift to higher energy compared to that of the pure Au metal, further confirming the strong chemical interaction between Au and MnO_2.[8]

We performed first principles calculations to study the electronic structure of Au-doped MnO_2 with two possible atomic configurations: Au-substituted and Au-interstitial spinel MnO_2 (Figure S4). As shown in Figure 2a and b, in both cases the electrons are found to transfer from the doped Au atoms to the surrounding O and Mn atoms. Thus, the oxidation state of the Mn atoms decreases because of the gain of electrons, which is consistent with the XPS measurements (Figure S3). From the total and partial density of states (DOS) obtained by hybrid density function theory (DFT) calculation (Figure S5), we can observe a band gap of about 2.5 eV in pure MnO_2, which is slightly larger than the previously reported value of about 1.7 eV.[9] For the Au-doped MnO_2, Au-induced gap states in MnO_2 can be clearly observed in the calculated DOS of two atomic configurations (Figure S5b and c), which are associated with Au d, O p, and Mn d orbitals. In Au-substituted MnO_2 (Figure S5b), the gap state is about 1.0 eV lower than the conduction band minimum (CBM) level in the majority-spin channel, which can act as a donor for an enhanced conductivity. In Au-interstitial MnO_2 (Figure S5c), the induced gap state is relatively broad in both majority- and minority-spin channels, while the gap with the CBM is quite small, inferring that the electrons in this gap state can be easily excited into the conductance band and contribute to the conductivity of MnO_2. In this calculation, the concentration of doped Au is about 2.0 at.%, lower than the experimental value. Therefore, the Au-induced gap states, associated with MnO_2 conduction, will have more overlap with CBM or larger mid gap states in real Au-doped MnO_2 that contains more Au and thus has a higher conductivity (Figure S6).

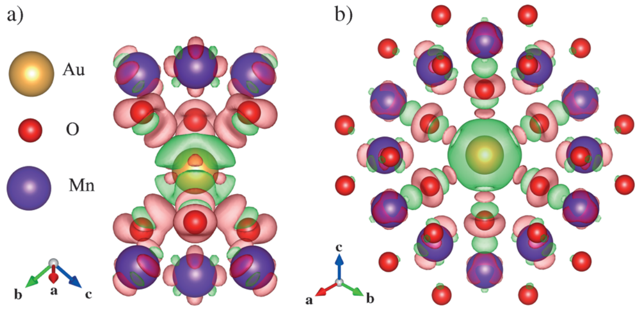

Figure 2. First principles calculation of Au-doped MnO_2. a) Differential charge densities of the Au-substituted MnO_2 and b) the Au-interstitial MnO_2. Green color indicates the loss of electrons whereas pink shows the gain of electrons.

The cross-section electronic conductivity of MnO_2 films with different Au doping was tested by a standard four-probe configuration (Figure S7). The concentrations of the dopant Au were controlled by the sputtering time. The electronic resistance of MnO_2 gradually decreases from 3.07 to 2.73 Ω (a reduction of about 11%) when the time for Au doping is up to 10 s (about 9.9 at.%; Figure S7b). Further increasing the Au doping from 10 to 20 s (about 18 at.%) leads to a slow decrease of resistance with about 4% loss. SEM images of the Au-doped MnO_2 films indicate that a longer sputtering time (> 10 s) results in the formation of a large number of Au nanoparticles (Figure S8), which may prevent Au atoms penetrating into the MnO_2 lattice. The fact that the conductivity of the films does not linearly increase with Au doping also implies that the conductivity enhancement of MnO_2 mainly arises from Au atom doping, rather than from Au nanoparticles.

The electrochemical measurements of the Au-doped MnO_2 films as electrodes were performed using a three-electrode system in a 2 M Li_2SO_4 solution. Figure 3a shows typical CV curves of the 9.9 at.% Au-doped MnO_2 electrode at scan rates from 5 to 100 mV s^{-1}. There is no obvious resistive behavior and the CV curves retain a symmetrical rectangular shape even at a scan rate of 100 mV s^{-1}. The capacitive performances of pure MnO_2 and Au-doped MnO_2 with a similar thickness (about 700 nm) but different Au doping amounts were studied. As shown in Figure 3b, the specific capacitance of the Au-doped MnO_2 is much higher than that of pure MnO_2. With the increase of the amount of doped Au, the specific capacitance first increases and then decreases slightly. The highest value is obtained for the 9.9 at.% Au-doped sample, which shows a 36% increment of the specific capacitance relative to pure MnO_2 at a scan rate of 5 mV s^{-1}. The reduction of the specific capacitance of MnO_2 with more Au doping may be due to the excessive gold nanoparticles, covering the surface of MnO_2 and prohibiting the reaction between MnO_2 and the electrolyte (Figure S8). With the increase of the MnO_2 film thickness, the advantage of Au doping becomes more obvious. When the thickness reaches about 1.35 μm (about 100 μg cm^{-2}), the specific capacitance of the pure MnO_2 film reduces to about 380 F g^{-1} at a scan rate of 5 mV s^{-1}, which is consistent with literature values.[10] Exceptionally, the specific capacitance of the Au-doped MnO_2 film with a similar thickness is as high as 626 F g^{-1} at a scan rate of 5 mV s^{-1}, which is over 65% higher than that of pure MnO_2 (Figure 3c) and is the best specific capacitance achieved from thick MnO_2 electrodes. Even the doped Au is counted into the total mass (Figure S9).

The cyclic voltammetry characterization of the pure MnO_2 and Au-doped MnO_2 electrodes were performed under the same electrochemical conditions used for the capacitor measurements. The capacitance of the pure MnO_2 gradually decreases during voltammetric cycling and the capacitance loss is about 34% after 15000 cycles while the capacitance of the Au-doped MnO_2 decreases first and increases then slightly. After 15000 cycles, a 7% increment of the capacitance is obtained (Figure 3d). To understand the underlying mechanism of the cyclic increment in the capacitance of the Au-doped MnO_2, the changes in the microstructure of the voltammetrically cycled pure and Au-doped MnO_2 electrodes were characterized by STEM and XPS. As

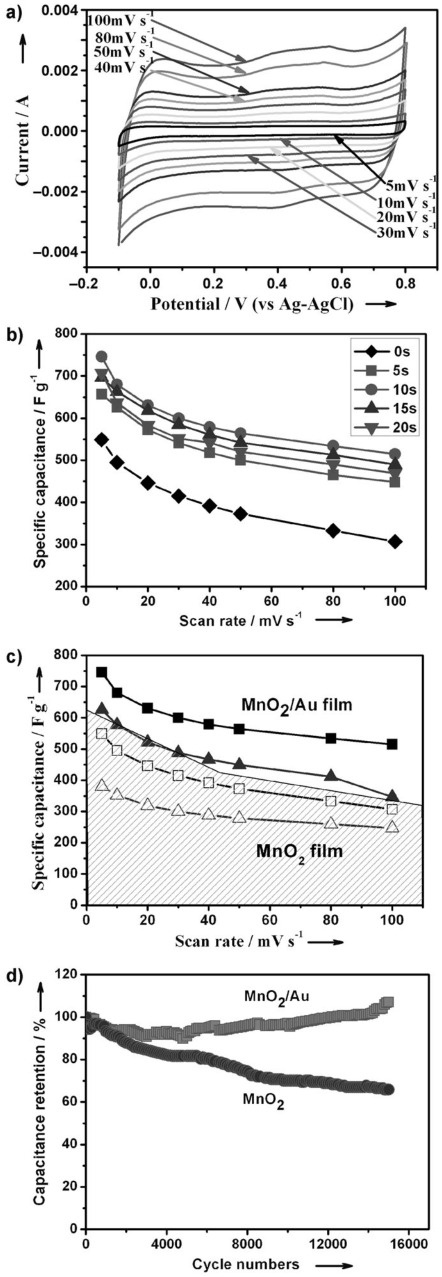

Figure 3. a) Typical cyclic voltammograms of 9.9 at.% Au-doped MnO$_2$ at different scan rates from 5 to 100 mV s^{-1} and b) the specific capacitance of Au/MnO$_2$ at different Au sputtering times based on the mass of MnO$_2$ versus the scan rates. c) Specific capacitance of pure MnO$_2$ and 9.9 at.% Au-doped MnO$_2$ with a thickness of about 0.7 μm (□ ■) and 1.35 μm (△ ▲). The solid symbols (■ ▲) represent Au-doped MnO$_2$ and the open ones (□ △) denote pure MnO$_2$. d) Cycling stability of pure MnO$_2$ and Au-doped MnO$_2$ electrodes with the same thickness of about 1.35 μm as a function of the cycle number. The measurement of the capacitance retention was carried out during cyclic voltammetry at a scan rate of 50 mV s^{-1}

shown in Figure S10, the voltammetric cycling leads to obvious changes in the morphology of both pure and Au-doped MnO$_2$. The as-prepared porous MnO$_2$ converts into a platelike structure, similar to previous observation.[11] It has been proposed that slow dissolution and re-deposition of MnO$_2$ occur simultaneously during electrochemical oxidation and reduction,[12] which is responsible to the morphology evolution of MnO$_2$ during cycling. Compared with the as-prepared MnO$_2$ (Figure S1), the cycled MnO$_2$ sheets become larger and thicker during voltammetric cycling, which may induce lower electron/ion transfer and thereby capacitance fading of pure MnO$_2$ because of the reduced effective surface areas and low electronic conductivity. Figure S10 c and d show STEM images of the Au-doped MnO$_2$ after voltammetric cycling. HAADF-STEM reveals that doped Au atoms have an increased number density and are distributed more uniformly in the cycled MnO$_2$, suggesting that electrochemical cycling gives rise to a homogenization of the doped Au during the dissolution–deposition process (Figure S10 d). It is also confirmed by XPS analysis that the high hydration of MnO$_2$, induced by Au doping, is still maintained after cycling (Table S2). Therefore, the homogenization of the doped Au atoms at the atomic scale can result in an enhanced conductivity and thus in a capacitance increment of Au-doped MnO$_2$.

In summary, the electronic conductivity of MnO$_2$ was obviously improved by non-equilibrium Au doping, which changes the electronic structure of MnO$_2$. The resultant thick Au-doped MnO$_2$ films possess an ultrahigh specific capacitance (626 F g^{-1} at a scan rate of 5 mV s^{-1}) and excellent cycling stability (7% increment after 15000 cycles). The excellent cyclic stability is even comparable to those of carbon-based electrochemical double-layer capacitors that are known to have the best cycling stability in electrochemical energy storage devices. The methodology developed in this study is not limited only to Au-doped MnO$_2$ but can be applied to many oxide materials to improve their electrochemical capacitance by enhancing their conductivity using non-equilibrium doping of free electron metals. Therefore, this study may pave a new way to improve the capacitive properties of transition-metal oxides for high-performance supercapacitors and batteries.

Experimental Section

Fabrication of Au-doped MnO$_2$ electrodes: The fabrication process of Au doped MnO$_2$ electrodes can be found in the Supporting Information. The concentration of the doped Au was calculated by at.% $= M_{\mathrm{Au}}/(M_{\mathrm{MnO_2}} + M_{\mathrm{Au}})100\%$, where M_{Au} and $M_{\mathrm{MnO_2}}$ were the molar weight of the doped Au and MnO$_2$ in the composite film. The thickness of the Au-doped MnO$_2$ was controlled by repeating the numbers of alternating deposition of MnO$_2$ and gold. The mass of the plated MnO$_2$ was determined by integration of the total coulombic charge used for plating over the duration of the electrolysis.[13]

Characterization of the microstructure: The microstructure of pure and Au-doped MnO$_2$ was investigated using a field-emission scanning electron mictroscope (SEM, JEOL JIB-4600F, 15 keV), a scanning transmission electron microscope (STEM, JEOL JEM-2100F) equipped with a double spherical aberration corrector for both the probe-forming and image-forming objective lenses. The electronic structure and oxidation states of the specimens were characterized by electron energy loss spectroscopy (EELS) and X-ray photoelectron spectroscopy (XPS, AxIS-ULTRA-DLD) with an Al Kα (mono) anode at an energy of 150 W in a vacuum of 10^{-7} Pa. A standard four-probe configuration was used for room-temperature resistance measurements.

DFT calculations: First principles calculations of Au-substituted and Au-interstitial spinel MnO_2 (Figure S2) were conducted by the projector-augmented-wave (PAW) based[14] Vienna ab initio simulation package (VASP)[15] within both the standard and hybrid DFT.[16] The structure relaxation was carried out within the general gradient approximation (GGA) in the Perdew–Burke–Ernzerhof (PBE) parameterization scheme[17] until the acting forces were smaller than 0.01 $eV\,Å^{-1}$. The density of states (DOS) was calculated based on the optimized structure using the HSE06 method[18] under consideration of the antiferromagnetic ordering of the spinel MnO_2.[9,19] The details of the calculations can be found in the Supporting Information.

Electrochemical characterization: All electrochemical tests were carried out using a three-electrode configuration. The distance between the working electrode and the counter electrode is about 2 mm. The cyclic voltammetry curves were measured in a potential range of −0.1–0.8 V at different scan rates in a 2 M Li_2SO_4 aqueous electrolyte. The cyclic stability was characterized by cyclic voltammetry measurements at a scan rate of 50 $mV\,s^{-1}$.

Received: November 9, 2012

Keywords: atomic doping · electrochemistry · electronic conductivity · MnO_2 · supercapacitors

---

[1] H. Y. Lee, J. B. Goodenough, *J. Solid State Chem.* **1999**, *144*, 220 – 223.
[2] a) S. C. Pang, M. A. Anderson, T. W. Chapman, *J. Electrochem. Soc.* **2000**, *147*, 444 – 450; b) J. N. Broughton, M. J. Brett, *Electrochim. Acta* **2004**, *49*, 4439 – 4446.
[3] C. Xu, F. Kang, B. Li, H. Du, *J. Mater. Res.* **2010**, *25*, 1421 – 1432.
[4] a) M. K. Song, S. Cheng, H. Chen, W. Qin, K. W. Nam, S. Xu, X. Q. Yang, A. Bongiorno, J. Lee, J. Bai, T. A. Tyson, J. Cho, M. Liu, *Nano Lett.* **2012**, *12*, 3483 – 3490; b) Y. Hou, Y. Cheng, T. Hobson, J. Liu, *Nano Lett.* **2010**, *10*, 2727 – 2733; c) X. Lu, T. Zhai, X. Zhang, Y. Shen, L. Yuan, B. Hu, L. Gong, J. Chen, Y. Cao, J. Zhou, Y. Tong, Z. L. Wang, *Adv. Mater.* **2012**, *24*, 938 – 944.
[5] a) X. Y. Lang, A. Hirata, T. Fujita, M. W. Chen, *Nat. Nanotechnol.* **2011**, *6*, 232 – 236; b) H. Zhang, X. Yu, P. V. Braun, *Nat. Nanotechnol.* **2011**, *6*, 277 – 281.
[6] a) J. Yan, E. Khoo, A. Sumboja, P. S. Lee, *ACS Nano* **2010**, *4*, 4247 – 4255; b) J. Liu, J. Jiang, C. Cheng, H. Li, J. Zhang, H. Gong, H. J. Fan, *Adv. Mater.* **2011**, *23*, 2076 – 2081.
[7] a) A. Aliev, M. Huvé, S. Colis, M. Colmont, A. Dinia, O. Mentré, *Angew. Chem.* **2012**, *124*, 9527 – 9531; *Angew. Chem. Int. Ed.* **2012**, *51*, 9393 – 9397; b) W. Wei, X. Cui, W. Chen, D. G. Ivey, *Chem. Soc. Rev.* **2011**, *40*, 1697 – 1721.
[8] W. S. Epling, G. B. Hoflund, J. F. Weaver, *J. Phys. Chem.* **1996**, *100*, 9929 – 9934.
[9] C. Y. Ouyang, Ž. Šljivančanin, A. Baldereschi, *J. Chem. Phys.* **2010**, *133*, 204701.
[10] a) P. Ragupathy, D. H. Park, G. Campet, H. V. Vasan, S. J. Hwang, J. H. Choy, N. Munichandraiah, *J. Phys. Chem. C* **2009**, *113*, 6303 – 6309; b) W. Wei, X. Cui, W. Chen, D. G. Ivey, *J. Phys. Chem. C* **2008**, *112*, 15075 – 15083.
[11] S. C. Pang, M. A. Anderson, *J. Mater. Res.* **2000**, *15*, 2096 – 2106.
[12] B. L. Wu, D. Lincot, J. Vedel, L. T. Yu, *J. Electroanal. Chem.* **1997**, *420*, 159 – 165.
[13] M. Nakayama, T. Kanaya, R. Inoue, *Electrochem. Commun.* **2007**, *9*, 1154 – 1158.
[14] a) P. E. Blöchl, *Phys. Rev. B* **1994**, *50*, 17953 – 17979; b) G. Kresse, D. Joubert, *Phys. Rev. B* **1999**, *59*, 1758 – 1775.
[15] a) G. Kresse, J. Hafner, *Phys. Rev. B* **1993**, *48*, 13115 – 13118; b) G. Kresse, J. Furthmüller, *Comput. Mater. Sci.* **1996**, *6*, 15 – 50.
[16] a) J. Heyd, G. E. Scuseria, *J. Chem. Phys.* **2004**, *120*, 7274 – 7280; b) V. Bayer, C. Franchini, R. Podloucky, *Phys. Rev. B* **2007**, *75*, 035404.
[17] J. P. Perdew, K. Burke, M. Ernzerhof, *Phys. Rev. Lett.* **1996**, *77*, 3865 – 3868.
[18] J. Paier, M. Marsman, K. Hummer, G. Kresse, I. C. Gerber, J. G. Ángyán, *J. Chem. Phys.* **2006**, *124*, 154709.
[19] D. Morgan, B. Wang, G. Ceder, A. Walle, *Phys. Rev. B* **2003**, *67*, 134404.